*Manuscript
Click here to view linked References

Efficient Numerical Methods for Multiple Surfactant-Coated Bubbles in a Two-Dimensional Stokes Flow

Mary Catherine A. Kropinski[a,*], Enkeleida Lushi[b,**]

[a] *Department of Mathematics, Simon Fraser University, Burnaby, British Columbia, Canada V5A 1S6*
[b] *Courant Institute of Mathematical Sciences, New York University, New York, New York, 10012*

Abstract

We present efficient and highly accurate numerical methods to compute the deformation of surfactant-coated, two-dimensional bubbles in a slow viscous flow. Surfactant acts to locally alter the surface tension and thereby change the nature of the interface motion. In this paper, we restrict our attention to the case of a dilute insoluble surfactant. The convection-diffusion equation for the surfactant concentration on the interface is coupled with the Stokes equations in the fluid domain through a boundary condition based on the Laplace-Young condition. The Stokes equations are first recast as an integral equation and then solved using a fast-multipole accelerated iterative procedure. The computational cost per time-step is only $O(N \log N)$ operations, with N being the number of discretization points on the interface. The bubble interfaces are described by a spectral mesh and is advected according to the fluid velocity in such a manner so as to preserve equal arc length spacing of marker points. This equal arc length framework has the dual advantage of dynamically maintaining the spatial mesh and allowing efficient, implicit treatment of the stiffest terms in the dynamics. Several phenomenologically different examples are presented.

Keywords: fluid interface, Stokes flow, insoluble surfactant, integral equations, bubbles, fast-multipole method.

*Supported in part by Natural Sciences and Engineering Research Council of Canada Grant RGPIN 203326
**Supported in part by the Applied Mathematical Sciences Program of the U.S. Department of Energy under Contract DEFG0200ER25053.
Email addresses: mkropins @ cs.sfu.ca (Mary Catherine A. Kropinski), lushi @ cims.nyu.edu (Enkeleida Lushi)

1. Introduction

Surface active agents (surfactants), whether present as impurities or deliberately added, critically alter the dynamics of multiphase flow systems. Surfactant molecules typically consist of hydrophilic heads and hydrophobic tails, and thus they tend to adhere to, and accumulate on, interfaces between fluids. Their impact is to locally lower the surface tension and thereby alter the dynamics, often critically. Important phenomenological effects that may be influenced by surfactant include bubble or droplet creation by tip streaming, cusp formation, and drop coalescence or breakup. Not surprisingly, surfactant can play an important role in many industrial and biomedical applications such as drug delivery, hydro-desulfurization of crude oil, polymer blending, paints and plastic production, emulsifications, or pulmonary functioning.

Computationally modeling these flows is very challenging. The interfacial surface tension depends on the surfactant concentration through a possibly-nonlinear equation of state. Nonuniform capillary (normal) and Marangoni (tangential) stresses are induced in the fluid, which significantly affects the deformation of the interface. The evolution equation for the surfactant concentration is stiff; surfactant diffuses by molecular mechanisms and is transported along the interface by fluid convection. There may be adsorption/desorption of interfacial surfactant to/from the bulk of the fluid. This evolution equation is coupled with the equations governing the fluid motion, and this coupling is highly nonlinear. The shape of the interface can become very complex: regions of high curvature might develop and/or topological changes may occur.

Numerically investigating the often-subtle phenomenological changes caused by the presence of surfactant (for example, whether a cusp forms in finite time, when and where surfactant caps form, the conditions required for tip streaming) clearly require a high degree of spatial and temporal accuracy. However, depending on the methods used, requiring higher accuracy may be achievable only at the expense of the size of problem that can be investigated. Even with significant advances in computer architecture, this trade-off continues to be negotiated. Recent examples in the literature support this point. Xu et al. [37] present a level set/immersed interface method for two-dimensional interfaces with insoluble surfactants. They present examples of up to four drops in a shear flow, with both a linear and nonlinear equation of state. Their methods include novel techniques to correct the characteristic loss of mass often seen in level set methods. However, even with these corrections, the change in drop area or surfactant mass can be up to 1%, with computational costs preventing the refinement needed for further accuracy. Integral equation methods are more amenable to numerical methods that can achieve high spatial accuracy, however, standard implementations [3, 26] can be very costly to compute. Not surprisingly, interfaces are often left under-resolved. For example [26] reports numerical oscillations in the interface shape due to inadequate spatial resolution and in [3], quantities were conserved to only 0.5%. The linearity of the Stokes equations can be exploited by a variety of analytic techniques. Seigel and coauthors [31] use slender-body theory to examine the conditions required for tip

streaming in a single axisymmetric bubble, presenting analytical results valid in certain regimes, only.

In this paper, we hope to provide motivation that when suitably chosen numerical methods are coupled with modern, fast, algorithms, it is possible to retain a high degree accuracy without sacrificing efficiency. Here, we present highly-accurate and efficient numerical methods for computing the motion of inviscid interfaces (bubbles) in a two dimensional Stokes flow in the presence of an insoluble surfactant. We employ integral equation methods based on the complex variable theory for the biharmonic equation and further developed by Kropinski [16, 17] for studying interfacial motion in a Stokes flow. The discretization of the integral equations is spectrally-accurate, and the iterative solution is accelerated by using the fast multipole method (FMM) [5, 27] to compute the matrix-vector products. With N points in the discretization of the boundary, the integral-equation solve requires only $O(N)$ operations, versus standard implementations of iterative schemes (for example [20]) which require $O(N^2)$ operations. For the motion of the interface, we employ the ideas of Hou et al. [13] and recast the evolution equations into an equal arc length frame. In this manner, we are able to dynamically maintain marker points at equal arc length intervals. More importantly, we can easily remove the stiffness caused by the diffusion term in the surfactant transport equation, since an implicit treatment of this term becomes explicit in Fourier space. The dynamics, then, are amenable to efficient treatment by high-order, semi-implicit methods such as the IMEX Runge-Kutta methods discussed in [2].

There are a variety of other analytical and computational approaches, each having their unique advantages and disadvantages. Integral equation methods are a natural choice for Stokes flow, and we are by no means the first to adopt this approach (a non-exhaustive list includes [3, 9, 20, 25, 39]). In most of these studies, a cubic spline or a lower-order representation is used to describe the interface. Siegel [29, 30] exploits the complex-variable theory for the biharmonic to derive analytical and semi-analytical methods (largely limited to studying a single bubble); these provide useful examples to verify other numerical methods. Methods that naturally handle topological changes (for example, drop breakup or coalescence) include level set and volume of fluid methods. For example, Xu et al. [37] use at a level set method to look at insoluble surfactants on droplets. Yang et. al [38] develop a hybrid level-set/front-tracking method to research interface problems for unstructured triangular grids. These methods are excellent for handling complicated, multi-component environments, but they tend to be low-order accurate. There has been recent work using the full Navier-Stokes equations [8, 18, 22]: however, these nascent studies are low-order accurate and simulations typically involve only a small number of bubbles or drops.

There are a number of limitations in the physical model we investigate here:

- It is in two dimensions.
- We do not consider the case of droplets containing fluid of a different viscosity.

- We consider the case, only, of insoluble surfactant with a linear constitutive relation between surfactant concentration and surface tension (although a nonlinear relationship can easily be substituted for the linear one).
- We cannot deal with topological changes.

While the physical model is limited, we believe our methods are useful for two reasons. First, our techniques are highly accurate and they will serve as a useful benchmark for other methods that are developed to solve more complicated models. Second, we feel this paper serves as a preliminary step in demonstrating the philosophy that by coupling modern fast algorithms with well-conditioned integral equations, it is possible to develop highly accurate and efficient tools for investigation problems of scientific interest. While the problems presented in this paper may be of limited scientific scope, currently, the methods can and will be extended to include, for example, three dimensions (the fast multipole method has already been adapted to handle the potentials associated with the Stokes equations in three dimensions [35]) and/or drops with different viscosity ratios ([16] includes this effect, albeit in the clean flow case, only).

We begin in the next section by outlining the governing equations for inviscid interfaces in a Stokes flow and the convection-diffusion equation for an insoluble surfactant. We show how the two are coupled through the Laplace-Young condition and an equation of state that relates surface tension to surfactant concentration. In section 3, we outline the complex variable theory for the biharmonic equation, and present the resulting integral equations for the problems at hand. The equal arc length framework is discussed in section 4, and we discuss the interface and surfactant dynamics in this framework. Our numerical methods are presented in section 5. In section 6 we use a semi-analytical solution of Siegel's [29] to verify our numerical methods. Further examples demonstrating a variety of different phenomena are given in section 7. In section 8, we state our conclusions.

2. The Governing Equations

2.1. The Fluid Dynamics

We consider the motion of a collection of two-dimensional closed fluid interfaces immersed in a slow viscous flow. The fluid domain is multiply connected, the interfaces enclose regions of an inviscid fluid, e.g. air, and are thus excluded from the flow domain, and is unbounded, or wall-bounded in extent (see figure 1).

We assume that the Reynolds number is small, thus the equations governing the fluid motion are the Stokes equations. Presented in their non-dimensional form, these are:

$$\nabla^2 \mathbf{u} = \nabla p, \qquad \nabla \cdot \mathbf{u} = 0, \qquad \mathbf{x} \in \Omega, \tag{1}$$

where $\mathbf{u} = (u, v, 0)$ is the fluid velocity and p is the pressure. Here, the variables have been scaled with respect to suitable characteristic values: length is the

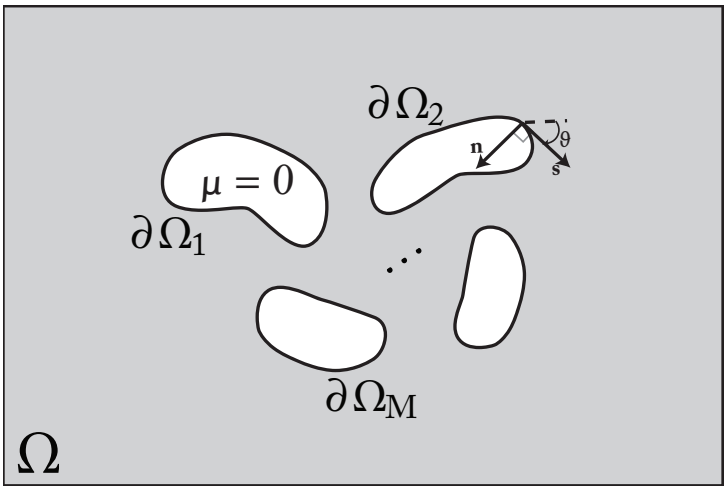

Figure 1: *A collection of bubbles in an unbounded viscous fluid domain Ω with boundary $\partial\Omega$. The component boundaries are denoted by $\partial\Omega_1$, $\partial\Omega_2, \cdots, \partial\Omega_M$. The unit normal $\mathbf{n}$ points out of Ω and θ is the tangent angle to Γ. The local curvature is given by $\kappa = \theta_s$, where s is arc length increasing in a clockwise direction.*

radius a of a typical bubble, velocity as σ_0/μ where σ_0 is the characteristic surface tension (the surface tension without surfactant) and μ is the kinematic viscosity (assumed to be constant), time as $a\mu/\sigma_0$, and pressure as σ_0/a.

The boundary condition on the interface is given by the Laplace-Young condition,

$$-(p - p_k)\mathbf{n} + 2\mathbf{E}\mathbf{n} = -\sigma\kappa\mathbf{n} + \nabla_s\sigma + \mathcal{B}\mathbf{n_g}\cdot\mathbf{x}, \qquad \mathbf{x} \in \partial\Omega_k, \tag{2}$$

where p_k is the internal pressure inside $\partial\Omega_k$ (effectively, this internal pressure ensures the area of each bubble remains constant, c.f. [17] for details). Here, $\mathbf{E}$ is the rate-of-strain tensor

$$E_{ij} = \frac{1}{2}\left(\frac{\partial u_i}{\partial x_j} + \frac{\partial u_j}{\partial x_i}\right),$$

where the indices i and j take on the values 1 or 2 corresponding to the x or y directions, respectively, σ is the (variable) surface tension and κ is the local curvature of $\partial\Omega$ (see figure 1 for orientation). The $\nabla_s\sigma$ term in (2) gives the tangential stress (Marangoni force), which results from the dependence of the surface tension on a nonuniform surfactant concentration. Gravity effects are included through the term containing the bond number $\mathcal{B}$, which is defined by

$$\mathcal{B} = \frac{\Delta(\rho - \rho^b)ga^2}{\sigma_0},$$

where ρ^b is the density of the inviscid fluid/gas in the bubble. Here, $\mathbf{n_g}$ is the unit normal pointing in the direction of gravity. We also require that the

following far-field conditions be satisfied:

$$\mathbf{u} \to \mathbf{u}_\infty, \qquad p \to p_\infty(t), \qquad \text{as } |\mathbf{x}| \to \infty.$$

We assume each $\partial\Omega_k$ is parametrized by $\alpha \in [0, 2\pi]$. For $\mathbf{x}(\alpha, t) \in \partial\Omega_k$, the motion of the interface is determined by integrating the following in time:

$$\frac{d\mathbf{x}(\alpha, t)}{dt} = U\mathbf{n} + T\mathbf{s}\,, \qquad \mathbf{x} \in \partial\Omega. \tag{3}$$

Here, the tangential velocity T is

$$T(\alpha, t) = T(0, t) - \int_0^\alpha \theta_{\alpha'} U d\alpha' + \frac{\alpha}{2\pi}\int_0^{2\pi} \theta_{\alpha'} U d\alpha', \tag{4}$$

where θ is the tangent angle to $\partial\Omega_k$ (again, see figure 1 for orientation). This choice for T maintains the *equal arc length frame*: $s_\alpha(t) = |\mathbf{x}_\alpha| = L_k(t)/2\pi$, where $L_k(t)$ is the total length of $\partial\Omega_k$ at time t. As discussed in [13, 16, 17], the equal arclength framework eliminates the need to post process the discretization points along the interface, and it prevents the stiffness exhibited when these points are allowed to cluster together. As we will see in the following section, it will also enable efficient temporal integration of the surfactant convection-diffusion equation.

2.2. The Surfactant Convection-Diffusion Equation

The non-uniformity of the surface tension σ arises from its dependence on the surface surfactant concentration Γ. This is given by an *equation of state* of the form $\sigma = \sigma(\Gamma)$. The relation between surface tension and surfactant concentration can be described by a logarithmic dependence called the Langmuir equation of state [9, 30, 37]. When the actual surfactant concentration is much lower than the closest packing case, i.e. the *dilute limit*, the equation of state can be approximated by a linear relationship (c.f. discussions in [24, 26, 37, 39]). Written in non-dimensional form, this relationship is

$$\sigma = (1 - \beta\Gamma), \tag{5}$$

where β is a non-dimensional constant expressing the sensitivity of the surface tension to the surfactant concentration; it is often called the elasticity parameter. We will use the linear equation here but note that the logarithmic one can be easily substituted in with no additional computational complication.

As shown in [32, 36], the evolution equation for an insoluble surfactant on an interface is

$$\frac{\partial\Gamma}{\partial t} = \frac{1}{Pe}\nabla_s^2\Gamma + \frac{d\mathbf{x}}{dt}\cdot\nabla_s\Gamma - \nabla_s\cdot(\Gamma(\mathbf{u}\cdot\mathbf{s})\mathbf{s}) + \Gamma(\nabla_s\cdot\mathbf{n})U, \qquad \mathbf{x} \in \partial\Omega_k. \tag{6}$$

The surfactant diffusion is controlled through the surface Peclet number,

$$Pe = \frac{\sigma_0 a}{\mu D_s},$$

where D_s is the surfactant diffusivity constant. We simplify (6) by observing that in two dimensions, $\nabla_s = \mathbf{s}\,\partial_s$. Let S be the tangential component of fluid velocity on $\partial\Omega$, $S = \mathbf{u}\cdot\mathbf{s}$, and recall from (3) that $\mathbf{s}\cdot d\mathbf{x}/dt = T$. Employing the Frenet formulae $\partial\mathbf{s}/\partial s = \kappa\mathbf{n}$, and $\partial\mathbf{n}/\partial s = -\kappa\mathbf{s}$ we obtain

$$\frac{\partial\Gamma}{\partial t} = \frac{1}{Pe}\frac{\partial^2\Gamma}{\partial s^2} + T\frac{\partial\Gamma}{\partial s} - \frac{\partial(\Gamma S)}{\partial s} - \kappa U\Gamma, \qquad \text{on } \partial\Omega_k.$$

Finally, rewriting this equation in terms of α gives

$$\frac{\partial\Gamma}{\partial t} = \frac{1}{Pe\, s_\alpha^2(t)}\frac{\partial^2\Gamma}{\partial\alpha^2} + \frac{T}{s_\alpha(t)}\frac{\partial\Gamma}{\partial\alpha} - \frac{1}{s_\alpha(t)}\frac{\partial(\Gamma S)}{\partial\alpha} - \kappa U\Gamma, \qquad \text{on } \partial\Omega_k. \quad (7)$$

3. The Sherman-Lauricella Integral Equations

Following the work in [16, 17], we reformulate the Stokes equations as integral equations based on complex variable theory for the biharmonic equation. The integral equations are essentially identical to those for the clean-flow problem, with minor modification to take into account variable surface tension. Below is a summary of the necessary details, and we refer the reader to [21, 23] for the development of this complex variable theory, and to [16, 17] for the application to the problems at hand.

The two-dimensional Stokes equations (1) can be simplified by introducing a stream function $\Psi(x, y)$ which satisfies the relations $u = \Psi_y$, $v = -\Psi_x$. The Stokes equations are then replaced by the biharmonic equation for $\Psi(x, y)$, $\Delta^2\Psi(x, y) = 0$. Any plane biharmonic function $\Psi(x, y)$ can be expressed by Goursat's formula as

$$\Psi(x, y) = \mathrm{Re}(\overline{z}\phi(z) + \psi'(z)),$$

where ϕ and ψ are analytic functions of the complex variable $z = x + iy$, and $\mathrm{Re}(f)$ denotes the real part of the complex-valued function f. All vectors, $\mathbf{n}$, $\mathbf{s}$, and $\mathbf{n_g}$ are replaced by their counterparts in complex variables n, s, and n_g, respectively. The functions $\phi(z)$ and $\psi(z)$ are known as Goursat functions, and all of the physical variables can be expressed in terms of these analytic functions. For completeness, we list them here (c.f. [19]):

$$\begin{aligned} i(u + iv) &= \phi(z) + z\overline{\phi'(z)} + \overline{\psi(z)}, \\ \zeta + ip &= -4\phi', \\ E_{11} + iE_{12} &= -E_{22} + iE_{21} = -i(z\overline{\phi''} + \overline{\psi'}), \end{aligned}$$

where $\zeta = -\Delta\Psi$ is the vorticity. In addition, for a point $\tau \in \partial\Omega_k$, the outward normal in the complex plane is given by $n = -i\tau_s$. An expression for the stress acting on the interface is

$$-(p - p_k)\mathbf{n} + 2\mathbf{E}\mathbf{n} \equiv -2\frac{\partial}{\partial s}\left(\phi - \tau\overline{\phi'} - \overline{\psi} + \frac{p_k}{2}\tau\right).$$

Substituting the above and $\kappa n = -\tau_{ss}$, $s = \tau_s$ into the interface condition (2) yields

$$\begin{aligned} -2\frac{\partial}{\partial s}\left(\phi - z\overline{\phi'} - \overline{\psi} + \frac{p_k}{2}\tau\right) &= \sigma\tau_{ss} + \sigma_s\tau_s - i\mathcal{B}\,\mathrm{Re}(n_g\overline{\tau}\tau_s) \\ &= \frac{\partial}{\partial s}(\sigma\tau_s) - i\mathcal{B}\,\mathrm{Re}(n_g\overline{\tau}\tau_s)\,, \qquad \tau \in \partial\Omega_k. \end{aligned}$$

Integrating the above with respect to s gives our final stress condition on the boundary:

$$\phi - z\overline{\phi'} - \overline{\psi} + \frac{p_k}{2}\tau = -\frac{1}{2}\sigma\tau_s + i\frac{\mathcal{B}}{2}\int_0^s \mathrm{Re}(n_g\overline{\tau}\tau_s)\,ds. \tag{8}$$

We note for future reference that the net force F_k acting on $\partial\Omega_k$ is related to the jump of the right-hand side of (8) about $\partial\Omega_k$. Specifically, this value is

$$F_k = -\mathcal{B}n_g A_k, \tag{9}$$

where A_k is the area bounded by $\partial\Omega_k$ (c.f. [17] for more details).

The suitable far-field expressions for the Goursat functions are

$$\phi \sim \phi_\infty(z) - \frac{i}{4}p_\infty(t)z + \frac{1}{2}G(t), \qquad \psi \sim \psi_\infty(z) - \frac{1}{2}\overline{G(t)}, \qquad \text{as } z \to \infty, \tag{10}$$

where the functions $p_\infty(t)$ and $G(t)$ are determined as part of the solution ($G(t)$ must be included to ensure that ϕ and ψ can be uniquely described). The functions ϕ_∞ and ψ_∞ are obtained from the far-field velocity:

$$\phi_\infty(z) + z\overline{\phi'_\infty(z)} + \overline{\psi_\infty(z)} = i(u_\infty + iv_\infty).$$

The integral equations are derived by finding suitable representations for $\phi(z)$ and $\psi(z)$. This is discussed extensively in [17], and we summarize these representations here:

$$\begin{aligned} \phi(z) &= \frac{1}{2\pi i}\int_{\partial\Omega}\frac{\omega(\xi,t)}{\xi - z}\,d\xi - \frac{i}{4}p_\infty(t)z + \phi_\infty(z) + G(t) \\ &\quad - i\frac{\mathcal{B}n_g}{8\pi}\sum_{m=1}^{M} A_m \log(z - z_m), \\ \psi(z) &= \frac{1}{2\pi i}\int_{\partial\Omega}\frac{-\overline{\omega(\xi,t)}\,d\xi + \omega(\xi,t)\,d\overline{\xi}}{\xi - z} - \frac{1}{2\pi i}\int_{\partial\Omega}\frac{\overline{\xi}\omega(\xi,t)}{(\xi - z)^2}\,d\xi + \psi_\infty(z) \\ &\quad - \overline{G(t)} + i\frac{\mathcal{B}}{8\pi}\sum_{m=1}^{M}\left\{\overline{n_g}A_m\log(z - z_m) + n_g A_m\frac{\overline{z}_m}{z - z_m}\right\}. \end{aligned}$$

In the above, logarithmic singularities have been placed at the centres z_k of each $\partial\Omega_k$. These singularities are *Stokeslet singularities*, and their strength is related to the total force acting on each bubble which, in turn, is given by (9). If $\mathcal{B} \neq 0$,

Stokes paradox results in a logarithmic growth of the velocity field. In order to eliminate the consequences of Stokes paradox, we follow the same approach that was taken in [10, 15, 17, 24] and assuming that the bubbles are embedded in a half space $\mathcal{S}$. By convention, we assume that $\mathcal{S}$ is the upper half plane so that a solid wall is placed at $y = 0$, and on this wall, the fluid velocity is zero. By changing the direction of gravity, n_g, it is trivial to change the relative position of the wall. The boundary condition on the wall is satisfied by using the method of images and formulae for the reflected sources are given in [15]. Effectively, the reflected Stokeslets act to cancel out the logarithmic growth of the velocity field.

Substituting these representations into (8), letting z tend to a point τ on the contour $\partial\Omega$ and using the classical formulae for the limiting values of Cauchy-type integrals, we obtain the Sherman-Lauricella integral equation,

$$\begin{aligned}\omega(\tau,t) + \frac{1}{2\pi i}\int_{\partial\Omega}\omega(\xi,t)\,d\ln\frac{\xi-\tau}{\overline{\xi}-\overline{\tau}} + \frac{1}{2\pi i}\int_{\partial\Omega}\overline{\omega}(\xi,t)\,d\frac{\xi-\tau}{\overline{\xi}-\overline{\tau}} - \frac{i}{2}(p_\infty - p_k)\tau \\ -\tilde{a}_k = -\frac{\sigma(\Gamma)}{2}\frac{\partial\tau}{\partial s} - \phi_\infty(\tau) + \tau\overline{\phi'_\infty(\tau)} + \overline{\psi_\infty(\tau)} + i\frac{\mathcal{B}}{2}\int_0^\alpha \mathrm{Re}(n_g\overline{\tau}\tau_{\alpha'})\,d\alpha' \\ + \frac{\mathcal{B}}{8\pi}\sum_{m=1}^{M}\left\{-2\ n_g A_m \arg(\tau - z_m) + i\overline{n_g}\frac{\tau - z_m}{\overline{\tau} - \overline{z_m}}\right\}, \qquad \tau \in \partial\Omega_k.\end{aligned} \tag{11}$$

Here, $\tilde{a}_k(t) \equiv a_k(t) - 2G(t)$, $p_\infty(t)$, and $p_k(t)$ are determined as part of the solution through

$$\begin{aligned}\tilde{a}_k &= -\int_{\partial\Omega_k}\omega(\xi,t)\,ds, \\ p_\infty(t) &= -\frac{2}{\pi}\mathrm{Re}\int_{\partial\Omega_1}\frac{\omega(\xi,t)}{(\xi - z_1)^2}\,d\xi, \\ p_k(t) &= p_\infty(t) + \frac{2}{\pi}\mathrm{Re}\int_{\partial\Omega_k}\frac{\omega(\xi,t)}{(\xi - z_k)^2}\,d\xi.\end{aligned}$$

4. Dynamics on the Interface

We now consider the motion of the interface. In order to reduce notational clutter, we assume below that $\tau \in \partial\Omega_k$, and that all variables and parameters are assumed to reside on the component curve under consideration. Much of what follows is discussed in depth in [16, 17] with minor modifications required to include variable surface tension.

Rewriting (3) in terms of complex variables yields

$$\frac{d\tau}{dt} = -Ui\frac{\tau_\alpha}{s_\alpha} + T\frac{\tau_\alpha}{s_\alpha}, \qquad \tau \in \partial\Omega_k, \tag{12}$$

where $U = \mathrm{Re}\{(u+iv)\overline{n}\}$ and

$$u + iv = -\frac{1}{2\pi} \oint_{\partial\Omega} \omega(\xi,t) \left\{ \frac{d\xi}{\xi - \tau} + \frac{d\overline{\xi}}{\overline{\xi} - \overline{\tau}} \right\} + \frac{1}{2\pi} \int_{\partial\Omega} \overline{\omega(\xi,t)}\, d\left(\frac{\xi - \tau}{\overline{\xi} - \overline{\tau}} \right) + u_\infty + iv_\infty + (u+iv)^s. \tag{13}$$

In the above, $\omega(\tau, t)$ is found from the solution to (11), and $\oint$ denotes a principal value integral. If gravity effects are included, it is understood that $(u+iv)^s$ takes on the value from the appropriate singular contributions.

Following the work of [13, 16], a small-scale decomposition of (3) yields

$$\frac{d\tau}{dt} \sim -\frac{1}{2} \frac{\mathcal{H}\left[\sigma(\Gamma)\tau_\alpha\right]}{s_\alpha(t)},$$

where $\mathcal{H}$ is the Hilbert transform. For explicit time-stepping methods, this will typically lead to a low-order stability constraint, $\Delta t = O(s_\alpha\, \Delta\alpha)$; however, it is clear that problems will arise when surface tension becomes small, which may happen in regions of large surfactant concentration. The diffusion term in (7) leads to a higher-order stability constraint, which is diagonalizable by the Fourier transform,

$$\frac{\partial \hat{\Gamma}(k)}{\partial t} = -\frac{k^2}{Pe\, s_\alpha^2(t)} \hat{\Gamma}(k) + \hat{R}(k), \tag{14}$$

where R contains the non-diffusive terms in (7), and $\hat{R}(k)$ is its Fourier transform. A similar approach was taken in [6] (albeit with a finite difference discretization) to study the effects of surfactant on capillary waves; to our knowledge it has not been applied to surfactant-laden interface motion in a Stokes flow.

Since the surfacant is insoluble, the total amount of surfacant on the interface must remain fixed,

$$\frac{d}{dt} \int_0^{2\pi} \Gamma(\alpha, t) s_\alpha(t)\, d\alpha = 0. \tag{15}$$

This is a constraint that is used to check the accuracy of our numerical solutions.

5. Numerical Methods

Using the methods outlined in [13, 16], we obtain a reparametrization of each component curve, $\tau \in \partial\Omega_k$, so that we achieve an initial equal arc length distribution of N_k marker points. We again label $\alpha \in [0, 2\pi)$ as the parameter; τ is uniformly discretized in α, where $h_k = 2\pi/N_k$ is the mesh spacing. All derivatives with respect to α are calculated spectrally via FFTs, and N_k is increased/decreased so as to maintain spectral resolution. At every time step, then, we are required to solve for N complex-valued unknowns, where $N = \sum_1^M N_k$. Below, we discuss the time integration schemes and in 5.2 we outline the spatial discretization.

5.1. Time Integration Schemes

The system of evolution equations can be written as

$$\frac{\partial}{\partial t}\begin{bmatrix} \tau \\ \Gamma \end{bmatrix} = \frac{1}{Pe}\begin{bmatrix} 0 \\ \frac{1}{s_\alpha^2}\frac{\partial^2 \Gamma}{\partial \alpha^2} \end{bmatrix} + \begin{bmatrix} E \\ R \end{bmatrix},$$

where E is the right-hand side of (12). We use IMEX (Implicit – Explicit) Runge-Kutta schemes that treat the first term on the right-hand side in the above implicitly, and the remainder explicitly. This is a natural choice, since the methods are self-starting and we anticipate that the diffusion term will be stiff. For most examples, we use the second-order Midpoint method found in [2] and which we denote by "RK2". For comparison, we also use a third-order scheme, which we call "RK3". More details on RK2 and RK3 can be found in [2]. Let Δt be the time step size and $(.)^n$ be the approximate solution at time $t = n\Delta t$. To implement RK2, then, we first obtain intermediate values

$$\begin{aligned} \tau^* &= \tau^n + \frac{\Delta t}{2} E^n, \\ \left[1 + \frac{\Delta t}{2}\frac{k^2}{Pe\,(s_\alpha^*)^2}\right]\hat{\Gamma}_k^* &= \hat{\Gamma}_k^n + \frac{\Delta t}{2}\hat{R}_k^n, \end{aligned} \tag{16}$$

where

$$s_\alpha^* = \frac{1}{2\pi}\int_0^{2\pi} |\tau_\alpha^*|\, d\alpha.$$

Final values are obtained through

$$\begin{aligned} \tau^{n+1} &= \tau^n + \Delta t E^*, \\ \Gamma^{n+1} &= \Gamma^{n+1} + \frac{\Delta t}{Pe\,(s_\alpha^*)^2}\frac{\partial^2 \Gamma^*}{\partial \alpha^2} + \Delta t\, R^*. \end{aligned} \tag{17}$$

Aliasing errors are suppressed using a high-order Krasny filter (c.f. [16, 17] for a more careful discussion on this point).

5.2. Discretization of the Integral Equation

In order to solve (11), we use the Nyström discretization based on the trapezoidal rule since it achieves super-algebraic convergence for smooth data on smooth boundaries. Associated with each such point $\alpha_j = (j-1)h_k$, $j = 1, \ldots, N_k$ on $\partial\Omega_k$, are the discrete variables τ_j^k, ω_j^k and Γ_j^k. The derivative values τ_α at α_j will be denoted by ν_j.

The discretization of the Sherman-Lauricella equation (11) is

$$\begin{aligned} \omega_j^k + \sum_{m=1}^{M}\sum_{i=1}^{N_m} K_1(\tau_j^k, \tau_i^m)\,\omega_i^m + \sum_{m=1}^{M}\sum_{i=1}^{N_m} K_2(\tau_j^k, \tau_i^m)\,\overline{\omega_i^m} + h_k \sum_{i=1}^{N_k} \omega_i^k \\ + i\frac{h_k \tau_j^k}{\pi}\sum_{i=1}^{N_k} \mathrm{Re}\left[\frac{\omega_i^k \nu_i^k}{(\tau_i^k - z_k)^2}\right] = g_j^k, \end{aligned} \tag{18}$$

where

$$g_j^k = -\frac{\sigma(\Gamma_j^k)}{2|\nu_j^k|}\nu_j^k - \phi_\infty(\tau_j^k) + \tau_j^k\overline{\phi_\infty'(\tau_j^k)} + \overline{\psi_\infty(\tau_j^k)} + i\frac{\mathcal{B}}{2}\int_0^{jh_k} \mathrm{Re}(n_g\overline{\tau^k}\tau_{\alpha'}^k)\,d\alpha'$$
$$+ \frac{\mathcal{B}}{8\pi}\sum_{m=1}^{M}\left\{-2\,n_g A_m \arg(\tau_j^k - z_m) + i\overline{n_g}\frac{\tau_j^k - z_m}{\overline{\tau}_j^k - \overline{z_m}}\right\}.$$

The discrete kernels K_1 and K_2 are given by

$$\begin{aligned} K_1(\tau_j^k, \tau_i^m) &= \frac{h_m}{2\pi i}\left(\frac{\nu_i^m}{\tau_i^m - \tau_j^k} - \frac{\overline{\nu_i^m}}{\overline{\tau_i^m - \tau_j^k}}\right), \\ K_2(\tau_j^k, \tau_i^m) &= \frac{h_m}{2\pi i}\left(\frac{\nu_i^m}{\overline{\tau_i^m - \tau_j^k}} - \frac{\overline{\nu_i^m}\,(\tau_i^m - \tau_j^k)}{(\overline{\tau_i^m - \tau_j^k})^2}\right). \end{aligned}$$

When $\tau_j^k = \tau_i^m$, K_1 and K_2 are replaced by the appropriate limits

$$\begin{aligned} K_1(\tau_j^k, \tau_j^k) &= \frac{h_k}{2\pi}\kappa_j^k|\nu_j^k|, \\ K_2(\tau_j^k, \tau_j^k) &= \frac{h_k}{2\pi}\kappa_j^k\frac{(\nu_j^k)^2}{|\nu_j^k|}, \end{aligned}$$

where κ_j^k denotes the curvature at the point τ_j^k.

As was done in [16, 17], the linear equations (18) are solved iteratively using a FMM-accelerated generalized minimum residual method GMRES [28]. Since the integral equations are Fredholm equations of the second kind, the number of iterations required to solve the system to a fixed precision is bounded; thus the total computational cost per time step is $O(N)$. Since the FFT is used to evaluate derivatives on the interface, the total cost is $O(N \log N)$.

Once the solution ω_j has been computed, we calculate the velocity at the grid points through discretizing (13):

$$u_j^k + iv_j^k = -\frac{h_k}{\pi}(\omega_\alpha)_j^k + \sum_{m=1}^{M}\sum_{i=1}^{N_m} K_1'(\tau_j^k, \tau_i^m)\,\omega_i^m + i\sum_{m=1}^{M}\sum_{i=1}^{N_m} K_2(\tau_j^k, \tau_i^m)\,\overline{\omega_i^m}$$
$$+ (u^s + iv^s)_j^k + (u_\infty + iv_\infty)_j^k, \tag{19}$$

where K_2 is defined previously and K_1' is

$$\begin{aligned} K_1'(\tau_j^k, \tau_i^m) &= -\frac{h_m}{2\pi}\left(\frac{\nu_i^m}{\tau_i^m - \tau_j^k} + \frac{\overline{\nu_i^m}}{\overline{\tau_i^m - \tau_j^k}}\right) \\ K_1'(\tau_j^k, \tau_j^k) &= -\frac{h_k}{2\pi}\mathrm{Re}\left\{\frac{(\nu_\alpha)_j^k}{\nu_j^k}\right\}. \end{aligned}$$

This quadrature rule is spectrally accurate and is based on subtracting off the singularity in the principal value integral. Again, FMM is used to evaluate (19).

Close Contact

As we will show in the following section, the above techniques are both efficient and accurate when the component curves $\partial\Omega_k$ are well separated from each other. However, when distinct interfaces come into close contact, the integral operators in (11) become close to singular. As discussed in [11, 12], the kernels can become under-resolved numerically even when the density and, in our case, the geometry of the interface are well resolved. Therefore, in addition to requiring an increase in N_k as the shape of the interface becomes more complex, we need to detect when component curves come into close contact and adapt accordingly. In [11, 12], an adaptive Gaussian quadrature was implemented to locally refine the mesh in regions of close contact between distinct component curves. We have found that in the context of moving interfaces, it is more efficient to adopt the procedure discussed in [15], which is to use the trapezoid rule but increase the number of discretization points sufficiently so that the kernels of the integral operators remain well resolved.

We now summarize this procedure. Let δ_{km} measure the distance of closest approach between bubble $\partial\Omega_k$ and $\partial\Omega_m$. As discussed in [15], in order to adequately resolve the interactions between these two bubbles, the following heuristic relationship between the mesh spacing and δ_{km} should be satisfied:

$$\max(ds_k, ds_m) < \frac{1}{4}\delta_{km}, \tag{20}$$

where ds is the mesh spacing measured in arc length, $ds_k = h_k s_\alpha$. At every time step, N_k is increased to ensure that the above is satisfied.

Care, of course, must be taken in order to ensure a particular configuration of bubbles satisfies (20). Finding δ_{km} between all particles by directly comparing the distances between all points would require $O(N^2)$ operations. Instead, we first embed the configuration of bubbles in a hierarchy of grid refinement. The first level of refinement is a single box which contains all of the bubbles. The next level in the hierarchy is achieved by subdividing each box in the current level into four regions; this subdivision continues until the width of a box at the finest level of refinement is just larger than $4\max_k ds_k$. All of the discretization points are then assigned to the boxes at this finest level. Determining whether or not (20) is satisfied reduces to checking this constraint in each non-empty fine box containing discretization points from different component curves. The computational cost for this is $O(N)$.

6. Semi-Analytical Solutions and Method Verification

In [33], complex-variable theory for the biharmonic equation is exploited in order to derive analytical solutions for a class of polynomial-shaped time-evolving bubbles with constant surface tension. In [29, 30], Siegel modifies these solutions to include surfactant effects. In this section, we summarize these semi-analytic solutions and use them to check the accuracy of our methods.

We focus on the simple case of an evolving elliptical bubble in a pure strain flow of the form $u \to (Qx, -Qy)$ as $|z| \to \infty$. (Here, Q is the dimensionless

strain rate, $Q = Q'\mu/\sigma_0$, where Q' is the dimensioned strain rate. The initial bubble shape is described by

$$z(\vartheta, 0) = a(0)e^{-i\vartheta} + b(0)e^{i\vartheta}, \qquad \vartheta \in [0, 2\pi],$$

where $a(0)$ and $b(0)$ are real and positive. The bubble area remains constant, $A(t) = \pi[a^2(t) - b^2(t)] \equiv A(0)$. As argued in [29], the bubble will evolve according to

$$z(\vartheta, t) = a(t)e^{-i\vartheta} + b(t)e^{i\vartheta}, \quad \vartheta \in [0, 2\pi].$$

The evolution of the parameters $a(t)$ and $b(t)$ are found through

$$\frac{d(ab)}{dt} = -2abI_0(a, b) + Qa^2, \tag{21}$$

where

$$I_0(a, b) = \frac{1}{4\pi}\int_0^{2\pi} \frac{\sigma(\Gamma(\vartheta', t))}{|z_{\vartheta'}(\vartheta', t)|} d\vartheta' \ .$$

Equation (21) is coupled to the surfactant concentration through the integral I_0. In this framework, the convection-diffusion equation for the surfactant becomes:

$$\frac{\partial \Gamma}{\partial t} = \frac{1}{Pe|z_\vartheta|}\frac{\partial}{\partial \vartheta}\left(\frac{\Gamma_\vartheta}{|z_\vartheta|}\right) + \mathrm{Re}\left(\frac{dz}{dt}\frac{\Gamma_\vartheta}{z_\vartheta}\right) - \frac{1}{|z_\vartheta|}\frac{\partial}{\partial \vartheta}\mathrm{Re}(P) + \frac{1}{|z_\vartheta|}\mathrm{Im}(\frac{z_{\vartheta\vartheta}}{z_\vartheta})\mathrm{Im}(P), \tag{22}$$

where

$$P(\vartheta, t) = \frac{\mathbf{u}}{|z_\vartheta|}\bar{z}_\vartheta\Gamma,$$

and

$$\begin{aligned} \mathbf{u} &= \frac{dz}{dt} - z_\vartheta e^{2i\vartheta}\left[\frac{1}{4\pi}\oint_0^{2\pi} \frac{\sigma(\Gamma(\vartheta', t))}{|z_\vartheta(\vartheta', t)|}\cot\left(\frac{\vartheta' - \vartheta}{2}\right) d\vartheta'\right] \\ &= \frac{dz}{dt} + z_\vartheta\frac{e^{2i\vartheta}}{2i}\mathcal{H}\left(\frac{\sigma(\Gamma)}{|z_\vartheta|}\right). \end{aligned}$$

The evolution of the surfactant coated bubble requires numerically integrating the evolution equations (21) and (22) given an initial bubble profile and distribution of surfactant, and for given values of β, Q and Pe. The surfactant concentration is represented spectrally with enough points to ensure full resolution, and we use a high-order Runge-Kutta method [4] for the time integration. Examples of initially circular bubbles in straining flow with two different strain rates are shown in figure 2 and figure 3. The lower strain rate, $Q = 0.15$, gives rise to a steady state, while a steady state does not exist for the higher strain rate (c.f. [29, 30] for a more thorough discussion on the phenomena resulting from different parameter values). We use Siegel's semi-analytic solutions to check the temporal errors in our numerical methods and the results are shown

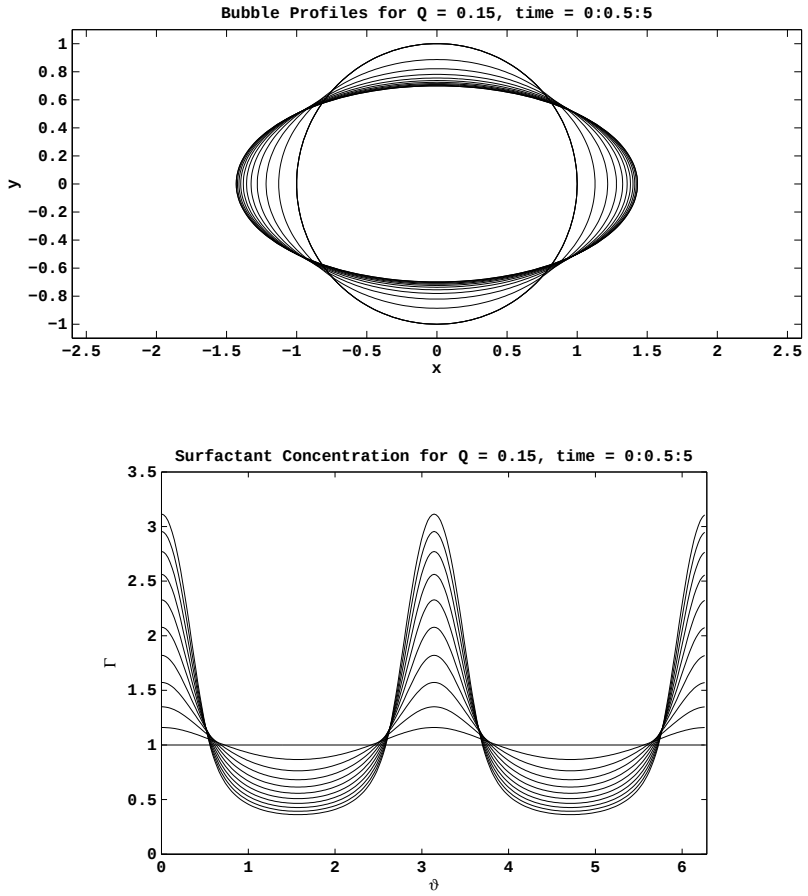

Figure 2: *Bubble profile and surfactant concentration for Siegel's semi-analytic solutions to a bubble in a straining flow,* $Q = 0.15$*,* $Pe = 10^3$*, and* $\beta = 0.1$*.*

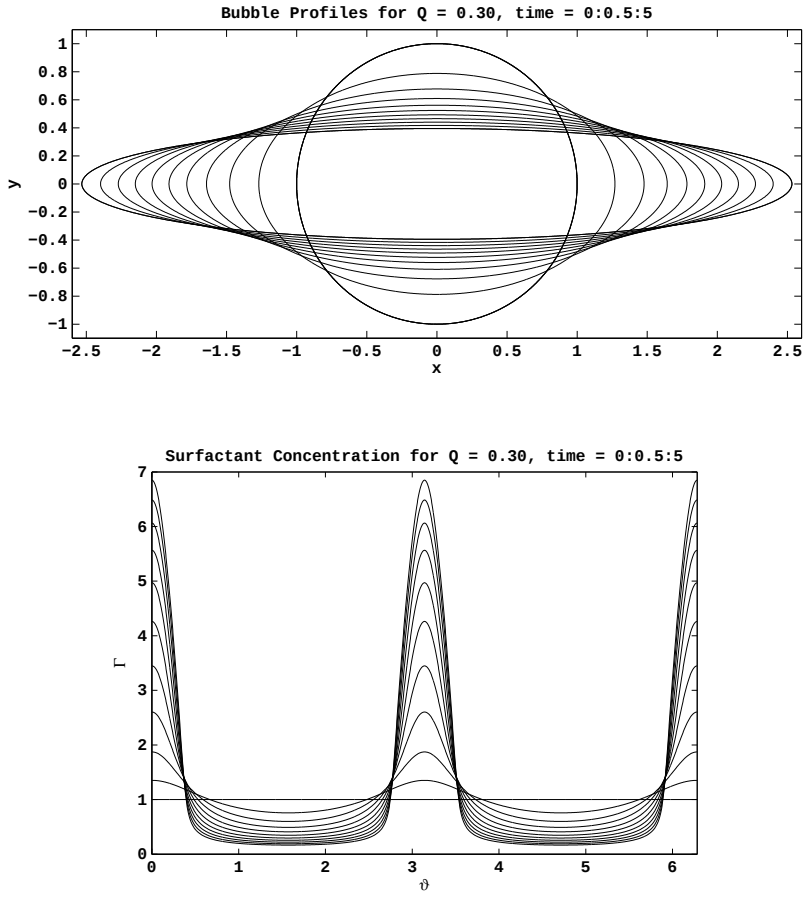

Figure 3: *Bubble profile and surfactant concentration for Siegel's semi-analytic solutions to a bubble in a straining flow,* $Q = 0.30$*,* $Pe = 10^3$*, and* $\beta = 0.1$*.*

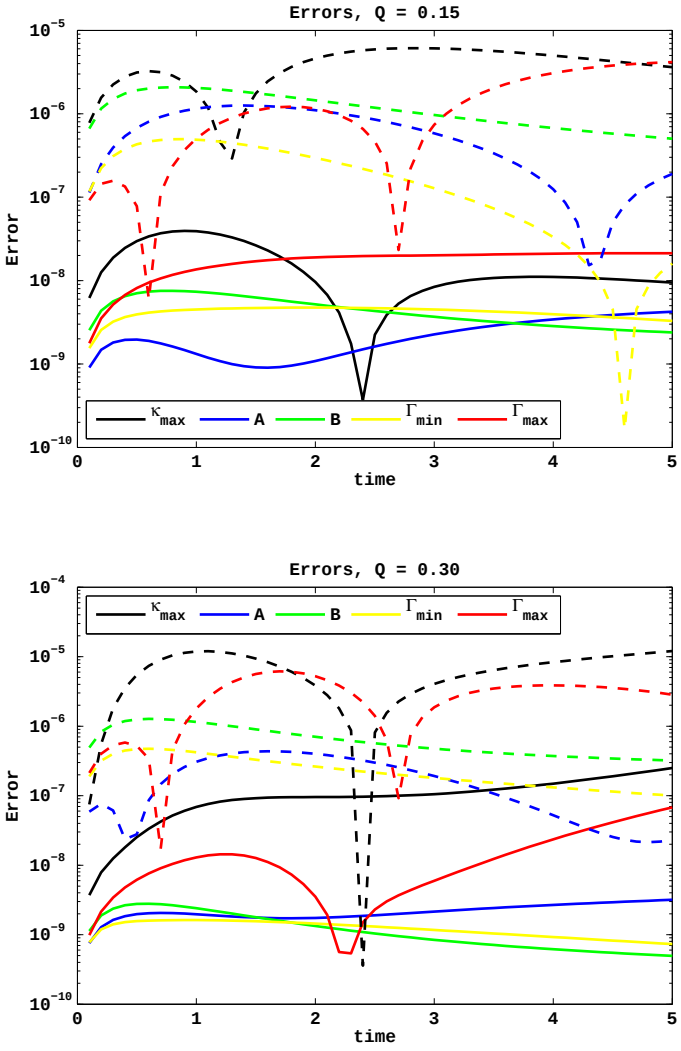

Figure 4: *Errors for the RK2 (dashed lines) and RK3 (solid lines). A and B are the ellipses' major and minor axes, respectively, and* $\kappa_{\max}$ *is the maximum curvature in absolute value. The figure on the left shows cumulated errors for* $Q = 0.15$ *(*$N = 256$*,* $\Delta t = 0.01$*, CPU time is 197 seconds for RK2, 301 seconds for RK3). The figure on the right is for* $Q = 0.3$ *(*$N = 2048$*,* $\Delta t = 0.005$*, CPU time is 1265 seconds for RK2, 1895 seconds for RK3). In both cases,* $Pe = 10^3$*,* $\beta = 0.1$*.*

in figure 4. In these simulations, N is large enough to ensure full spatial resolution. Two time integrators are used: RK2 and RK3 (c.f. Section 5.1), and the errors in the total surfactant concentration and in the bubble geometry are shown in figure 4. With a time step $\Delta t = 0.01$, RK2 keeps all errors to $O(10^{-5})$ or below. Furthermore, errors in mass and surfactant conservation remain on or below $O(10^{-4})$. For RK3 and with an initial time step of 0.005, the errors are $O(10^{-7})$, with mass and surfactant being conserved to, at worst, $O(10^{-6})\%$. We also use this example to show the linear scaling of the computational costs with N in table 1.

N	CPU Time
128	7.16
256	12.76
512	22.06
1024	39.45
2048	74.26

Table 1: The CPU time in seconds required to compute the bubble profile and surfactant concentration for Siegel's semi-analytic solutions for a bubble in a straining flow, $Q = 0.15$, with $Pe = 10^3$ and $\beta = 0.1$, and for increasing values of N. In each, $\Delta t = 0.01$, and the final time was $t = 2.0$.

7. Numerical Results

In this section we illustrate the strengths of our numerical methods with a variety of examples demonstrating different phenomenological effects. In all examples, N^k is kept sufficiently large to ensure full spatial resolution. The algorithms have been implemented in Fortran and the tolerance for GMRES is set to at most 10^{-10}. As a measure of error, we track any loss in area or surfactant concentration. Unless otherwise stated, these errors are below 10^{-3}. All timings cited are for a single processor on a Mac Pro with a quad-core Intel Xeon processor.

Bubbles in a Linear Straining Flow

It has been widely studied, both experimentally and mathematically (e.g. in [34, 29]), that for a range of parameters β, Pe, and Q, a bubble placed in a linear strain flow will reach an elliptical steady-state profile. In this steady-state regime, it is possible for the surfactant to be entirely swept to the bubble tips and eventually form stagnant *surfactant caps*. Examples of steady surfactant-covered bubbles at two different strain rates are shown in figure 5.

Figure 6 shows an example of two bubbles in a linear straining flow. The two bubbles are initially placed so that the are separated by a distance of 0.4. As the bubbles evolve, a dimpling region forms between the two bubbles. As shown in figure 7, the size of this dimpled region is influence by surfactant. It is interesting to note that as β increases, not only does the height of the dimpling

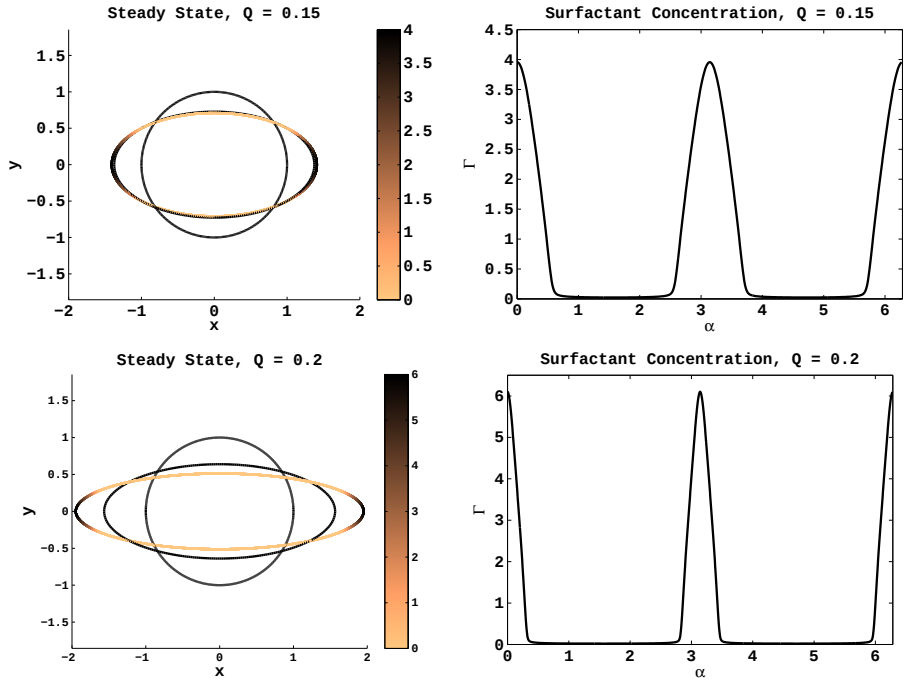

Figure 5: *Stable surfactant caps for* $Q = 0.15$ *and* $Q = 0.2$, $Pe = 10^3, \beta = 0.1$. *The surfactant caps are shown clearly at the bubble tips.*

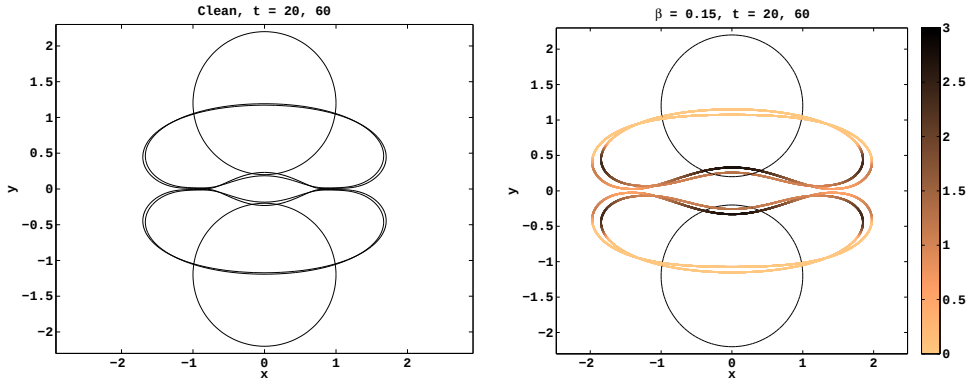

Figure 6: *Two bubbles in a linear straining flow,* $Q = 0.2$, *at* $t = 0$, $t = 20$, *and* $t = 60$. *The plot on the left is the clean flow example (CPU time to* $t = 20$ *was 52.2 minutes, to* $t = 60$ *was 58 hours,* $N = 8192$ *at* $t = 60$*), and on the right,* $Pe = 10^3$, $\beta = 0.15$ *(CPU time to* $t = 20$ *was 12.7 minutes, to* $t = 60$ *was 186.0 minutes,* $N = 2048$ *at* $t = 60$*).*

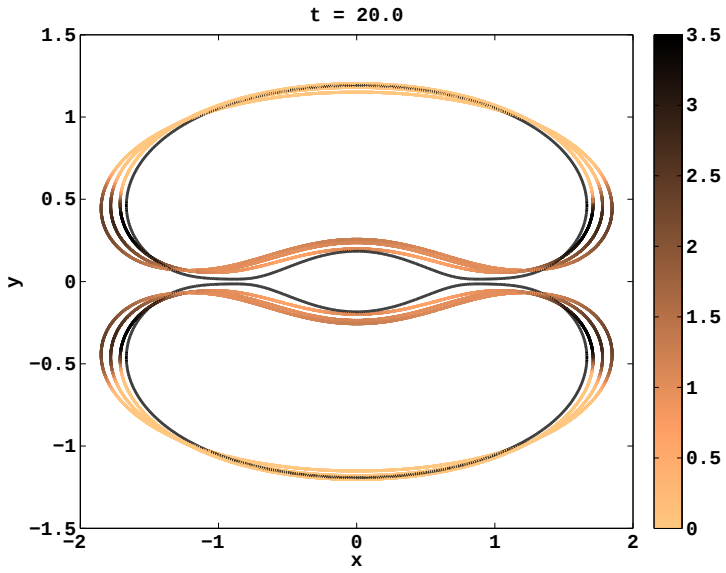

Figure 7: *Two bubbles in a linear straining flow, $Q = 0.2$, at $t = 20$ for $\beta = 0$, 0.05, 0.10, 0.15 (least through most deformed, respectively).*

region increase, but so does the minimum separation between the two interfaces. A summary of this effect is shown in table 2.

	$\Delta y_{\min}$		Δy_d	
β	$t = 20$	$t = 60$	$t = 20$	$t = 60$
0.00	0.029	0.014	0.368	0.463
0.05	0.110	0.032	0.398	0.614
0.10	0.127	0.040	0.472	0.643
0.15	0.137	0.053	0.514	0.659

Table 2: Separation distances for the example of two bubbles in a shear flow; $\Delta y_{\min}$ measures the minimum distance between the two interfaces near the tips and Δy_d measures the height of the dimpled region.

Bubbles in a Cubic Straining Flow

In an experimental setup with a bubble placed in the middle of a four roller mill, G.I. Taylor witnessed that at a critical rotation rate of the rollers, the bubble achieved pointed ends [34]. This phenomenon was further investigated by De Bruijn [7], who showed that jets or small bubbles may be emitted from these pointed tips in a process called *tip streaming*. De Bruijn's experiments suggest that tip streaming occurs when gradients in surface tension develop.

Antanovskii [1] showed that the four-roller-mill plane flow employed by Taylor is described, to leading order, by the following far-field velocity and pressure

fields:

$$\mathbf{u}_\infty = Q(x,-y) + Q\epsilon(x^3+3xy^2,-3x^2y-y^3), \qquad P_\infty = p_\infty + 6Q\epsilon(x^2-y^2).$$

These correspond to the following far-field expressions for the Goursat functions

$$\phi_\infty = -\frac{i}{2}Q\epsilon z^3, \quad \psi_\infty = -iQz.$$

Hear, Q is the linear nondimensional strain rate, and $Q\epsilon$ is a low-order, additional, rotational strain rate. Due to the presence of a cubic term in ϕ_∞, this type of flow is often called cubic-strain flow.

β	$\max N$	CPU Time
0.00	2048	2.6
0.05	4096	5.9
0.10	8192	18.9
0.15	32768	406.3

Table 3: The CPU time in minutes and the final value of N ($N = 1024$ initially) required to compute the cubic straining flow examples up to $t = 2.5$. Here, $Q = 0.3$, $Pe = 10^3$. In each, the initial time step is $\Delta t = 0.005$. This time step is cut in have each time N is doubled (N is increased so as to maintain spectral resolution).

The stability of the resulting spindle-like bubble shapes are studied in [25, 30]. For a range of parameters the surface tension force is inadequate to balance the outward motion of the bubble, hence the profile becomes unstable. Here we present numerical examples to demonstrate this. The response to different values of β for a single strain rate $Q = 0.3$ is shown in figure 8. This figure also shows the corresponding surface tension on the interface. (To make a better comparison, we follow [25] and rescale the non-dimensional surface tension by $\sigma = (1-\beta\Gamma)/(1-\beta)$. This ensures that for all values of β, $\sigma(1) = 1$.) The surfactant has accumulated at the bubble tips, lowering the surface tension there.

Further details of the time evolution of different quantities are shown in figure 9. In this figure, we plot the evolution of the deformation of the bubble, defined by:

$$D = \frac{R_{\max} - R_{\min}}{R_{\max} + R_{\min}},$$

where $R_{\min}$, $R_{\max}$ are the minimum and maximum values of the bubble radius, respectively, as well as maximum normal velocity of the fluid, the curvature at the tip, and the ratio of maximum to minimum surfactant concentration. Finally, a comparison of the tip at different values of β is shown in figure 10.

The above examples demonstrate that our numerical methods can track the time-evolution of such shapes far into cusp formation (we have accurately tracked increases in tip curvature up to $O(10^3)$). A detailed study of the stability of the cusped bubbles for different parameters Q, Pe, β, and ϵ, or the role of a